10 Wall heat flux calculations from temperature measurements

10.1 Introduction

The operating principle of the dual thin film probe is described in this chapter, emphasizing on the wall heat fluxes calculations from the wall temperature measurements provided by the two thin film sensors. Curvature effects on the heat conduction phenomenon inside the substrate of the gauges are discussed in detail. The importance of the accurate knowledge of the values of the thermal products ratio of the two substrates for accurate gas temperature calculations is underlined. Moreover, the experimental determination of the thermal products ratio is presented.

10.2 Operating principle

Two platinum thin film sensors (with a resistance of about *60Ω*) are each located at the stagnation point of the hemispherical head of two Macor (ceramic) cylinders (Figure 1-3). These thin films act as variable resistance thermometers; the change of their resistance is monitored by means of a constant current Wheatstone bridge (*W/B*) (see Appendix 18.1). For temperatures ranging between ambient and *390K*, the sensor temperature – resistance relationship can be verified as linear, without any loss on accuracy. The *W/B* is a standard tool for high accuracy measurements of small resistance changes. The sensitivity of the *W/B* is directly proportional to the value of the current passing through the thin film. On the other hand, the resulting, undesired, Joule heating of the gauge is proportional to the square of this current. The optimum value of the current of the VKI W/B used for the experiments with the dual thin film probe was found to be of the order of *6-7mA*. For this current intensity, the temperature increase of the thin film sensor due to the Joule effect is less than *1K*, and the VKI W/B output is acquired between *0* and *2.5V* for the test conditions in the cascade facility, CT2 (chapters 11 and 12). Buttsworth and Jones (1998a) utilized *20mA* current, while Denos (1996) suggests that the current of the *W/B* connected to a cold wire should be kept below *2mA*, for a *2.5 μm* wire with length to diameter ratio equal to 220.

A resistance placed inside of one of the Macor cylinders allows its heating before the test. The probe measurement principle is based on the operation of the two thin film sensors at different temperatures (T_{W1}, T_{W2}). Since the two gauges are nominally identical, if they are exposed to the same flow, the values of the convective heat transfer coefficient are the same (Eq. (44)) and the total flow temperature is determined from Eq. (45):

$$Q_{W1} = h\left(T_{GAS} - T_{W1}\right),\ Q_{W2} = h\left(T_{GAS} - T_{W2}\right)\ , \tag{44}$$

$$T_{GAS} = T_{W1} + \frac{T_{W1} - T_{W2}}{Q_{W2} / Q_{W1} - 1}\ . \tag{45}$$

The definition of the heat transfer coefficient h in its general form for low and high velocity flows, as well as for fluids characterized by a Prandtl number different than *1*, is based on the adiabatic wall temperature T_{AW} instead of the total gas temperature T_{GAS} (see Eq. (44)). However, as the heat transfer coefficient h is measured at the stagnation point for the two hemispherical heads, the adiabatic wall temperature T_{AW} coincides with the total gas temperature T_{GAS}. For the next study, the temperature T_{GAS} is simply referred as gas temperature, calculated from Eq. (45). More information about the definitions of the two above-mentioned temperatures is given in appendix 18.5. Also, note that for the measurements with the dual thin film probe the measured T_{GAS} corresponds to the real gas temperature contrary to the thermocouple measurements, where the measured T_{GAS} corresponds to the recovery temperature. The assumption that both ceramic heads feel the same flow at the same time during the real experimental conditions is discussed in paragraph 15.4.

In Equation (44), the two wall heat fluxes (Q_{W1}, Q_{W2}) are calculated from the time history of the measured wall temperatures, recorded by the thin films. The signal processing is based on the solution of the one dimensional conduction equation inside the hemispherical substrates and the wall heat flux is computed from the temperature gradient at the wall (Fourier law).

10.3 One dimensional heat conduction

As already mentioned in paragraph 3.2, the thin film thickness (which is of the order of *0.2μm*) does not affect the temperature history of the substrate surface. The heat conduction (during the test) is taken into account across the substrate radius (*1.5mm*), while the lateral conduction effects are considered negligible (Buttsworth and Jones, 1997). The one dimensional heat conduction equation is expressed in Eq. (46) in radial coordinates (r):

$$\frac{\partial}{\partial r}\left[k(T)\frac{\partial T}{\partial r}\right]+k(T)\frac{\sigma}{r}\frac{\partial T}{\partial r}=\rho c(T)\frac{\partial T}{\partial t}\ , \qquad \text{[Eq. (40) repeated*]} \qquad (46)$$

where σ is equal to 0 for a flat plate, 1 for a cylinder and 2 for a sphere and k stands for the thermal conductivity, ρ for the density, c for the specific heat and R for the radius of the substrate. This expression contains:

a) important curvature effects, when the heat penetrates until a depth of the order of the radius of curvature,

b) thermal property variations within the substrate when the wall temperature changes by more than *100K*. (Miller, 1981, gives the dependence of the bulk thermal properties of Pyrex 7740, quartz and Macor with temperature.)

The first boundary condition (*B.C.*) results from the symmetry condition applied at the center of the substrate (Eq. (47) for $r=0$). This *B.C.* allows a wall heat transfer solution to be obtained even after the heat has penetrated until the center of the substrate. However, the measurement time is usually selected to be small enough, so that the heat does not reach the center and the substrate stays semi-infinite during the tests. The second *B.C.* is the wall temperature history, measured by each gauge (Eq. (48) for $r=R$). The initial condition is the initial temperature of each gauge and, therefore substrate, before the test:

$$\left(\frac{\partial T}{\partial r}\right)_{r=0,\,t}=0\ , \qquad \text{[Eq. (41) repeated*]} \qquad (47)$$

$$T\left(r=R,t\right)=T_W\left(t\right)\ . \qquad (48)$$

The heat flux at the wall is computed by means of the Fourier law:

$$Q_W\left(t\right)=-k\left(T\right)\left(\frac{\partial T(t)}{\partial r}\right)_{r=R}\ . \qquad \text{[Eq. (42) repeated*]} \qquad (49)$$

10.4 Numerical solution for the radial heat conduction

To the author's knowledge, there is no analytical solution that describes the transient wall heat flux around a cylinder or a sphere, neither for constant wall heat flux, nor for constant fluid temperature, nor for any other kind of boundary condition. Thus, Eq. (46) can only be solved numerically; it is transformed from second to first partial derivative of r, by using the auxiliary derivative u (Buttsworth, 1997):

---

* Note that Eq. (40) is applied at the stagnation region of the blade that is approximated to a cylinder (*σ=1*), while Eq. (46) is applied at the stagnation region of the hemispherical heads of the dual thin film probe (*σ=2*). Also, the center of the substrate in Eq. (41), (42) stands for *r=R*, while the wall for *r=0*.

$$\frac{\partial}{\partial r}\left[k(T)\cdot\frac{\partial T}{\partial r}\right]=\frac{\partial u}{\partial r}\ . \tag{50}$$

The discretization of this term uses the points (*M+1/2*) and (*M-1/2*) around point (*M*), (Figure 10-1). The conductivity *k* is averaged between points (*M+1*) and (*M*), or (*M*) and (*M-1*) respectively. The second term of Eq. (46) is discretized at points (*M+1*) and (*M-1*) around the point (*M*). This leads to a second order scheme in the *r* – direction:

$$\frac{\partial u}{\partial r}=\frac{u_{M+1/2}-u_{M-1/2}}{\Delta r},\frac{\partial T}{\partial r}=\frac{T_{M+1}-T_{M-1}}{2\Delta r},u_{M+1/2}=k_{M,M+1}\frac{T_{M+1}-T_{M}}{\Delta r},\ u_{M-1/2}=k_{M-1,M}\frac{T_{M}-T_{M-1}}{\Delta r}. \tag{51}$$

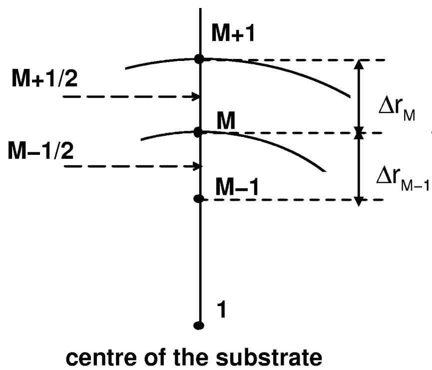

Figure 10-1: Discretization on r-direction

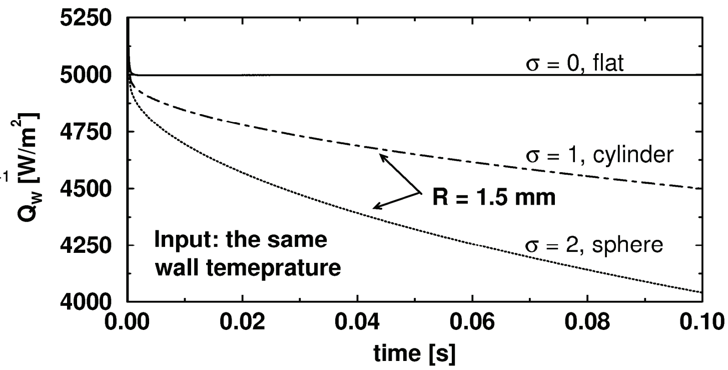

Figure 10-2: Curvature effects on the wall heat flux calculations

The values of the temperature and the thermal properties of the substrate are taken at the time step where the temperature distribution along the substrate is known. The right hand side of Eq. (46) is discretized in forward time with a first order accuracy. At each time step (e.g. t_1), the solution (e.g. $T(r,t=t_1)$) is given for every value of *r*. Combining all the terms leads to Eq. (52) and to the solution of a tri-diagonal matrix, which is a fast way of solving an implicit method scheme:

$$A_M T_{M-1}^{P+1}+B_M T_M^{P+1}+C_M T_{M+1}^{P+1}=T_M^{P}\ . \tag{52}$$

For the above analysis, the total number of grid points used in the *r* – direction is *5000* for a substrate radius of *1.5mm*, and the time step is equal to $10^{-4}s$. The code was also tested for smaller time steps, where the number of grid points was also increased. The grid can eventually be refined in the stagnation area, where the temperature gradients are more important.

The importance of the first derivative of the temperature with respect to *r* in Eq. (46) that takes into account the curvature effects of the substrate is illustrated in Figure 10-2: the boundary condition of Eq. (48) is the wall temperature history that is numerically reconstructed to correspond to that of a step in wall heat flux for a flat geometry (Eq. (9)). The numerical solutions (for $\sigma = 0,1,2$) of Figure 10-2 demonstrate *10%* and *20%* difference between the wall heat flux of a cylinder and a flat plate or a sphere and a flat plate respectively after *0.1s* of application of the above wall temperature history, for a radius of *1.5mm*. The last remark becomes more important for the next study as the radius of the ceramic heads of the VKI dual thin film probe is also equal to *1.5mm*; thus, an accurate calculation of the two wall heat fluxes (Q_{W1}, Q_{W2}) for an accurate gas temperature determination (Eq. (45)) during a test should be based on conduction in radial coordinates (Eq. (46)) that takes into account the curvature effects of the two substrate heads. Also, note that for all the wall heat flux calculations for the next series of experiments, the value of the thermal product is chosen equal to $2073J/(m^2Ks^{0.5})$; the latter value is representative for ceramics (Macor) and is suggested after several calibrations by Denos (1996).

The influence of the radius on the wall heat flux is shown in Figure 10-3: the wall heat flux that corresponds to a cylinder is represented with long-short dashed lines and that to a sphere with long dashed lines; the different colors correspond to different values of the radius. The smaller the radius gets, the more important the curvature effects become. Especially, around the value of *1.5mm* radius, the wall heat flux calculation can be significantly influenced. Only for 10 times higher values (*15mm* radius), the difference of the wall heat flux between sphere (or cylinder) and flat plate starts to become negligible (e.g. a difference of *7.2%* and *3.6%* respectively at *0.5s* of the experimental time). The influence of the different values of the substrate diameters on the gas temperature calculations can be found in paragraph 15.2.

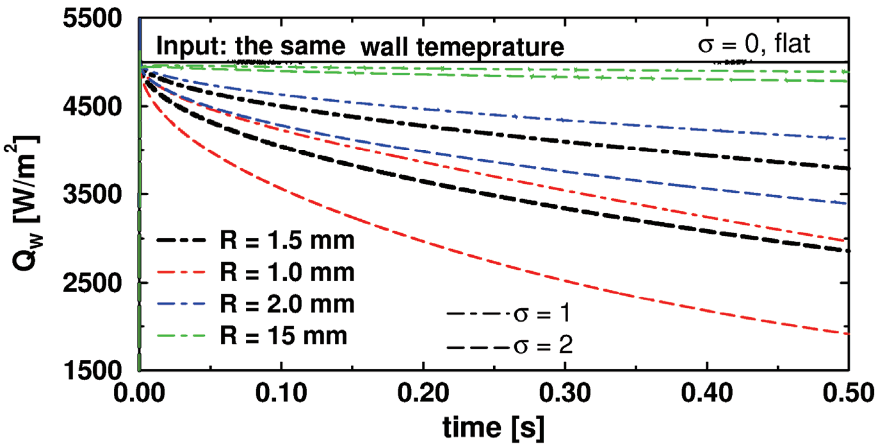

Figure 10-3: Influence of the radius on the wall heat flux calculations

10.5 Analytical approximation for the radial heat conduction

An analytical approximation of the wall heat flux calculation was suggested by Buttsworth and Jones (1997): the wall heat flux was obtained on the basis of a semi-infinite flat plate analysis ($Q_{W,FP}$) and then was corrected for curvature effects (Eq. (37)). It is valid only when the heat penetrates a relative small distance into the substrate such that $at/R^2 << 1$.

The accuracy of Eq. (37) is better than *1%* for configurations typically encountered in transient heat transfer testing provided $at/R^2 < 0.06$ (where a stands for the thermal diffusivity, t for the experimental time and R for the substrate radius). A comparison between the output of the numerical solution and the above approximation of the wall heat flux is presented in Figure 10-4 for $R=1.5mm$. The agreement is within *2.5%* for cylinders and less than *1%* for spheres for testing times below *0.4s* (Iliopoulou and Arts, 2002).

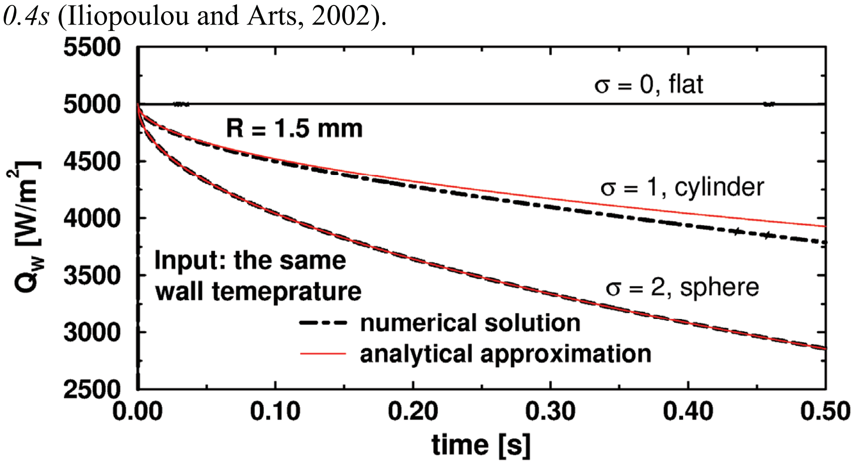

Figure 10-4: Comparison between the numerical solution and the analytical approximation of the wall heat flux

10.6 Noise on the gas temperature calculations

The most significant difficulty of these measurements is that small noise on the sensor temperature signals during the tests results in high noise on the reconstructed heat fluxes. This amplification of the noise:
a) is somehow expected as the wall heat flux is proportional to the wall temperature space-derivative (Eq. (49)),
b) is supported by the wall heat flux analytical solution in the Laplace domain based on the heat conduction for a flat geometry (Eq. (8)).

Furthermore, the variables which create the highest noise on the calculation of the gas temperature seem to be the two wall heat fluxes. This fact requires a strong low pass filter on the temperature signals of the two gauges, prior to the gas temperature calculations. In an attempt to define the magnitude of the error introduced on the gas temperature calculation, a numerical analysis was undertaken by considering periodic numerically constructed temperature signals, submitted, in addition, to a random numerical noise (Iliopoulou and Arts, 2002).

In a first step (Figure 10-6), two parabolic evolutions of the two wall temperatures are generated for each gauge, by using the solution that corresponds to that of a step in wall heat flux for flat geometry (Eq. (9)).

The second step of the analysis is the introduction of an oscillation on the gas temperature signal. This is made by superposing constant magnitude oscillations of specific period (equal to $1/f_{OS}$, where f_{OS} stands for the frequency of the oscillations) on the above wall temperature histories. The magnitude of these oscillations should of course be such that the resulting heat transfer coefficients of the two sensors are exactly the same. The magnitude of the temperature fluctuations of the cold gauge (gauge 2) results therefore from the one of the hot gauge (gauge 1). The equations which are used for the construction of the periodic gas temperature signal are (Eq. (53), (54), (55)):

$$Q_{W1} = f\left(T_{W1} + \Delta T_{W1}\right),\ \ Q_{W2} = f\left(T_{W2} + \Delta T_{W2}\right) \qquad \text{(Numerical solutions),} \qquad (53)$$

$$Q_{W1} = \left(h + \Delta h\right)\left[T_{GAS} + \Delta T_{GAS} - \left(T_{W1} + \Delta T_{W1}\right)\right] \qquad \text{(Conduction on gauge 1),} \qquad (54)$$

$$Q_{W2} = \left(h + \Delta h\right)\left[T_{GAS} + \Delta T_{GAS} - \left(T_{W2} + \Delta T_{W2}\right)\right] \qquad \text{(Conduction on gauge 2),} \qquad (55)$$

where ΔT_{W1}, ΔT_{W2} and Δh are the oscillations of the two temperature histories and of the corresponding heat transfer coefficient. The final step is the superposition of numerically generated random noise on the T_{W1} signal ($0.005K$). The average value of this random noise is zero.

Four different cases of numerically generated periodic signals with a $0.005K$ noise are examined in the following paragraphs; the selected parameters for each case are listed in Table 10-1. The main two parameters (whose influence on the gas temperature calculations is studied) are the wall heat fluxes ratio (Q_{W1}/ Q_{W2}) and the sampling frequency (f_S). The values of all the parameters are based on representative values from experiments.

	f_S [kHz]	T_{W1}^{INIT} [K]	Q_{W1}/ Q_{W2}	$(\Delta T_{W1})_{MAX}$ [% of total change in 0.5 s]
Case 1	5	305	0.737	2
Case2	5	330	0.079	17.5
Case 3	10	305	0.737	2
Case 4	10	330	0.079	17.5
	f_{OS} [Hz]	T_{W2} [K]	T_{GAS}^{AV} [K]	$(\Delta h)_{MAX}$ [% of total change in 0.5 s]
All Cases	50	295	333	5

Table 10-1: Parameters for the four cases of the numerical generated periodic signals

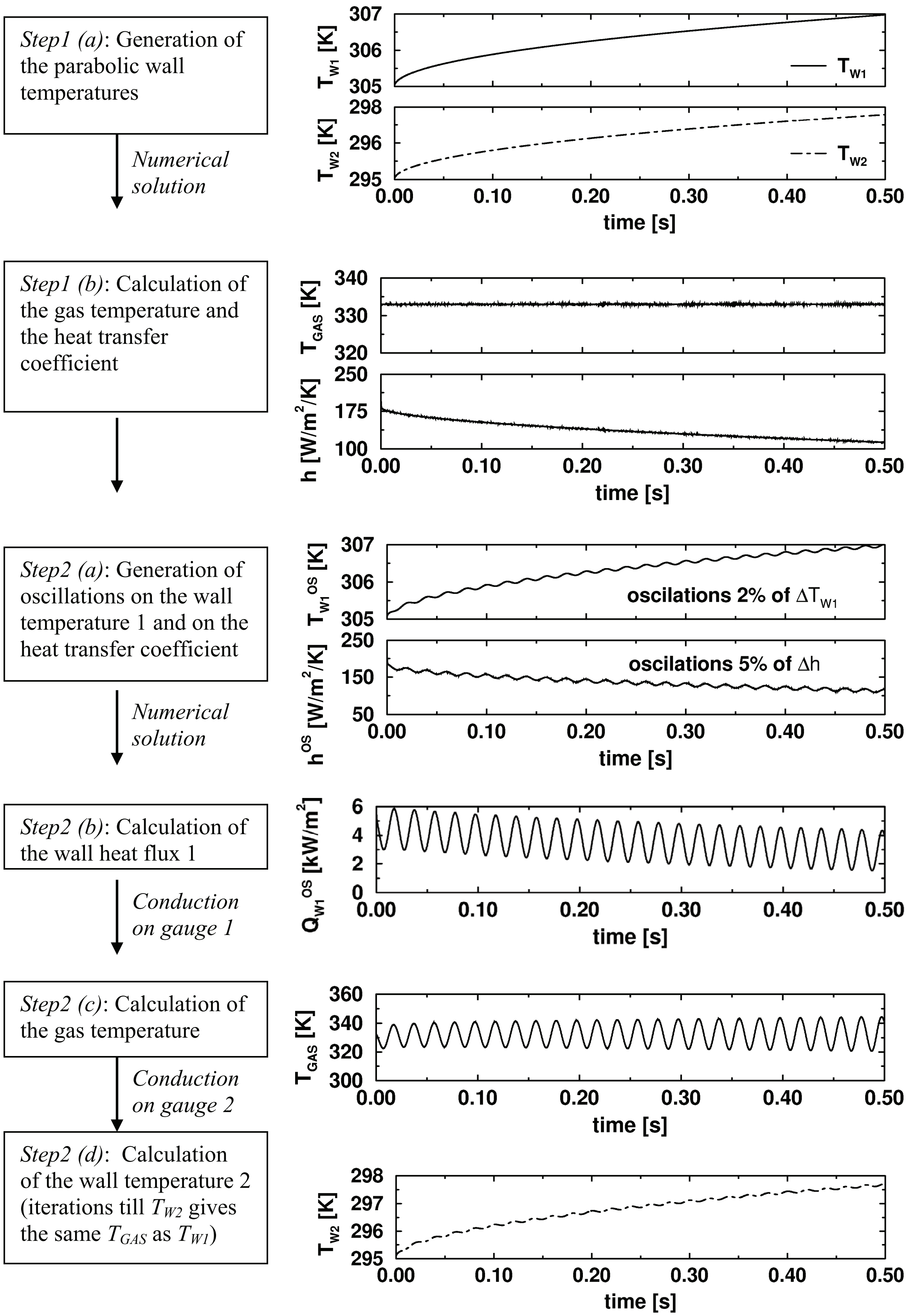

Figure 10-5: Procedure of the numerically generated periodic signals

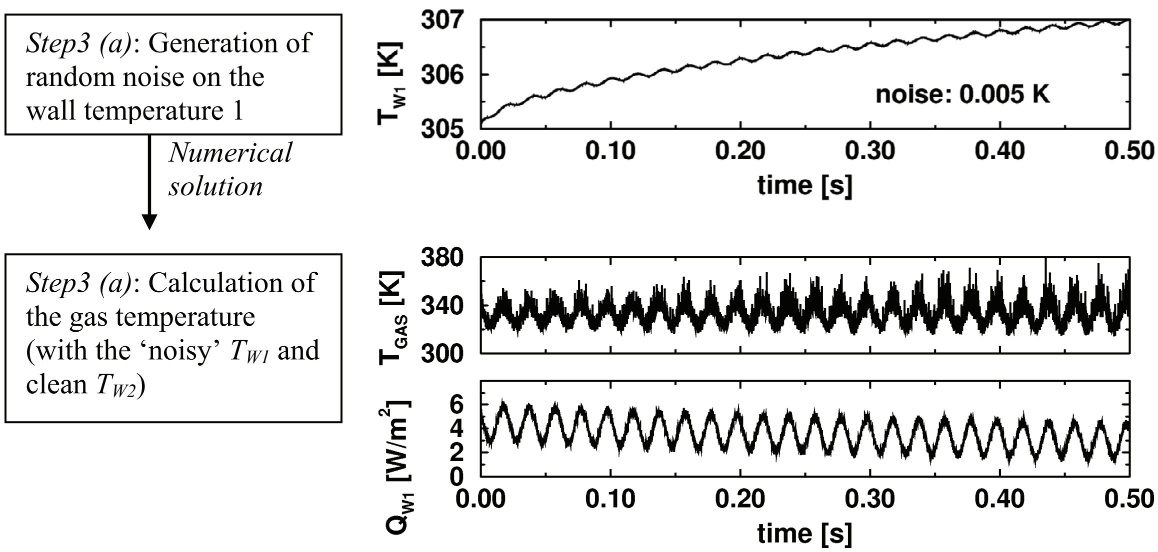

Figure 10-6: Superimposition of random noise on the numerically generated periodic signals

The first case of the numerically generated periodic signals with noise *0.005K* on T_{W1} is shown in Figure 10-7. On the first top graph, the wall heat flux history of the first gauge (Q_{W1}) with noise is shown. It is obvious that the generated noise is about one order of magnitude less important than the periodic value of the heat flux. On the middle graph, the gas temperature, which corresponds to the periodic with noise temperature history of the hot gauge (T_{W1}) and the periodic temperature history of the cold gauge (T_{W2}), is shown. A maximum noise of *0.005K* on the one of the two wall temperature signals introduces about *40K* noise on the gas temperature signal. The ratio of the two corresponding wall heat fluxes (Q_{W1}/Q_{W2}) with respect to time is shown in the third graph, where the maximum noise is more than *10%* of the total signal. This noise on the wall heat fluxes ratio contributes therefore in a major way to the noise on the gas temperature (Eq. (45)). Thus, a second numerical case is studied; the wall heat fluxes ratio is brought close to zero, by bringing the initial wall temperature of the first gauge (T_{W1}^{INIT}) close to the gas temperature. The amplitude of the oscillations on the temperature signals and the heat fluxes, as well as the average values of the gas temperature and the wall temperature of the cold head are kept the same with the first case.

The second case is illustrated in Figure 10-8; the noise on the gas temperature (middle graph) is four times reduced compared to the first case only by bringing the wall heat fluxes ratio close to zero. The latter remark is one of the most important conclusions of this numerical analysis and it is used on the real experimental applications of the probe, whenever it is possible.

The choice of the parameters of the third case is the same as that of the first case, expect that the sampling frequency is doubled from *5kHz* (case1) to *10kHz* (case3). The top graph of Figure 10-9 reveals that the calculated heat flux is depended on the sampling frequency. The higher the sampling frequency, the higher the noise on the heat flux calculations and inevitably on the gas temperature calculations (middle graph). There is tremendous increase of noise by just using double value of the sampling frequency on the gas temperature signal whose noise is increased by *25K*!

The influence of the sampling frequency on the gas temperature calculations for low wall heat flux ratio is shown in Figure 10-10. As the sampling frequency of case4 is doubled (*10kHz*) compared to case2 (*5kHz*), the noise on the gas temperature of case4 is also almost double. However, as the wall heat fluxes ratio is close to zero, the total noise on gas temperature is limited to *15K*. Therefore, during the real experimental environment, it is advisory that the sampling frequency is chosen not higher than the needed one for the correct resolution of the signal.

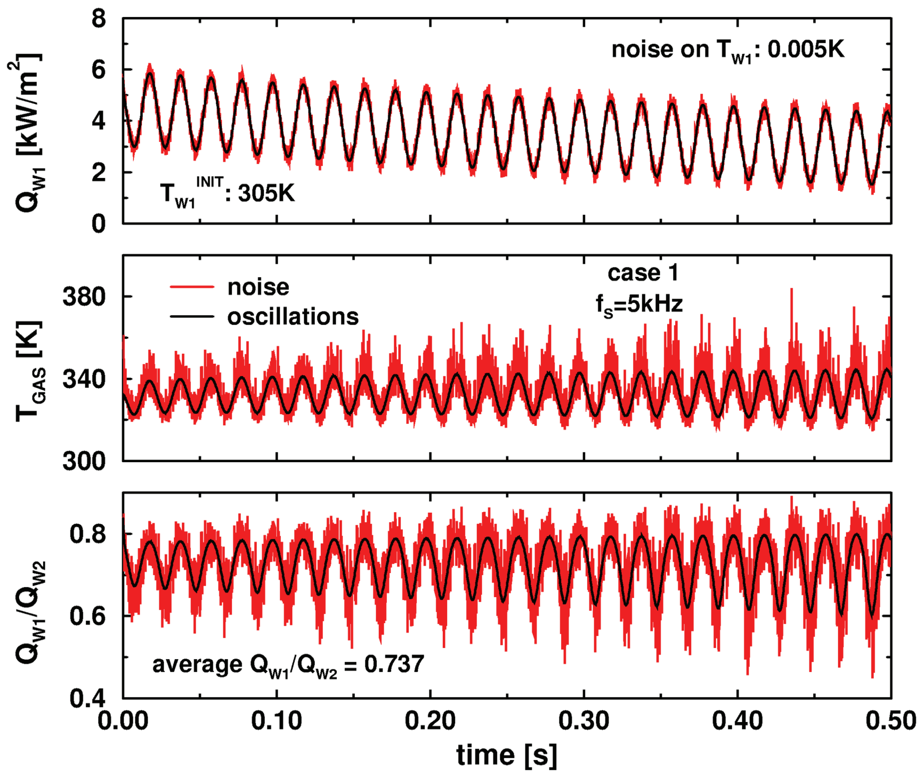

Figure 10-7: Case 1; high heat flux ratio introduces high noise on the gas temperature calculations

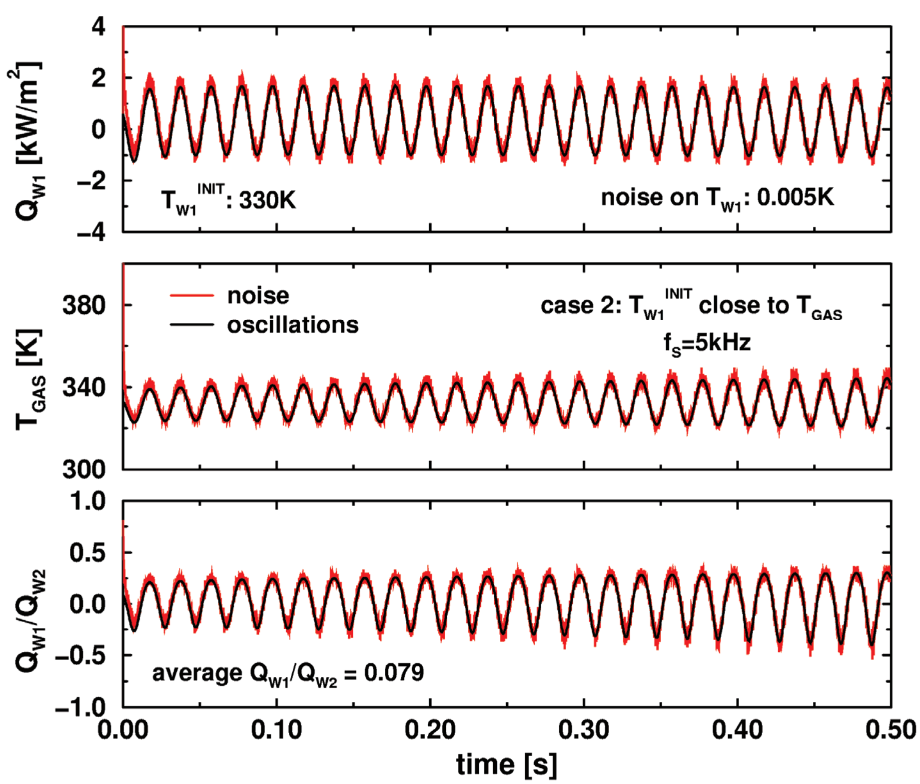

Figure 10-8: Case 2; reduced noise on the gas temperature calculations by decreasing the heat flux ratio

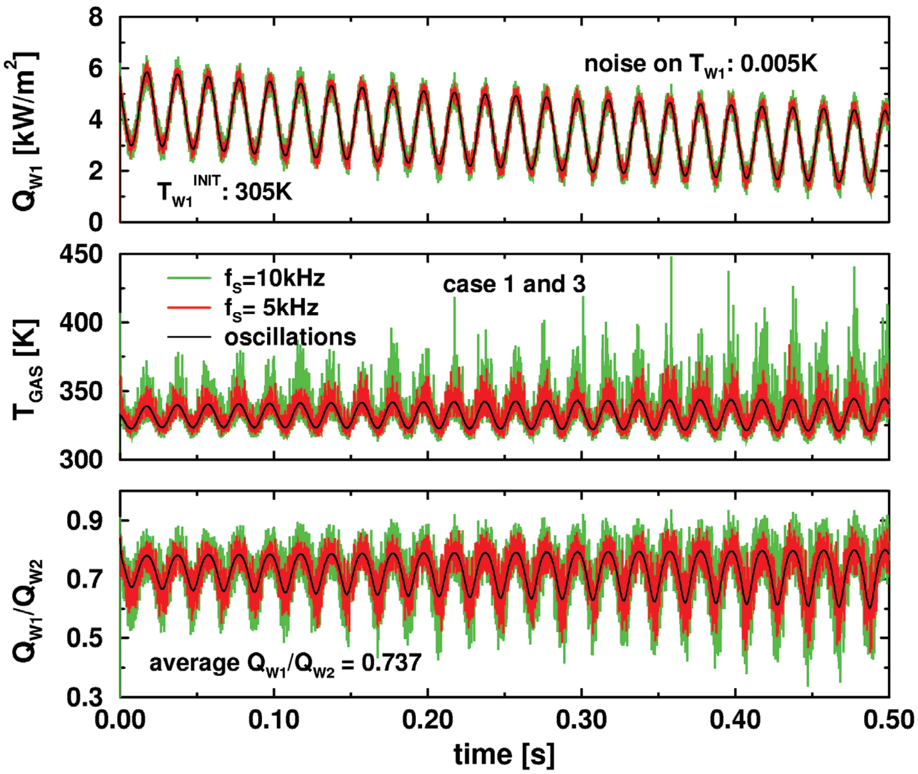

Figure 10-9: Case 3; influence of the sampling frequency on the gas temperature calculations for high wall heat flux ratio

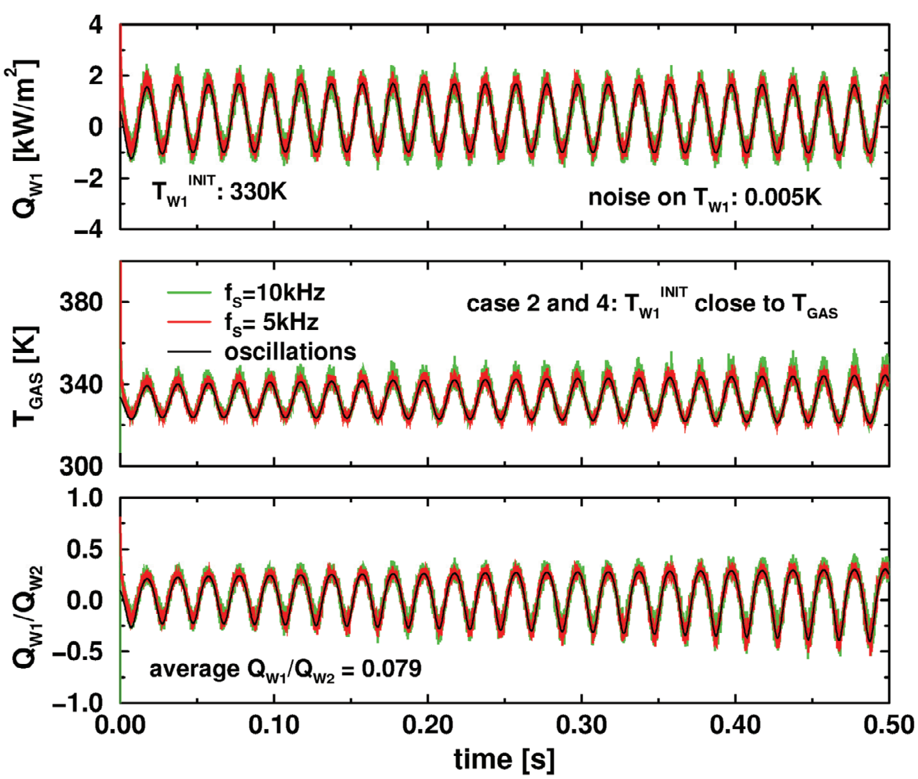

Figure 10-10: Case 4; influence of the sampling frequency on the gas temperature calculations for low wall heat flux ratio

If the measured freestream temperature would, physically, exhibit a periodic behavior, a phase locked averaging procedure (*PLA*) would largely suppress this problem. This is demonstrated in Figure 10-11, where a *PLA* on 24 periods of the wall temperature signal (T_{W1}) for the cases with the high wall heat flux ratio reduces the total noise to about *5K* for both cases.

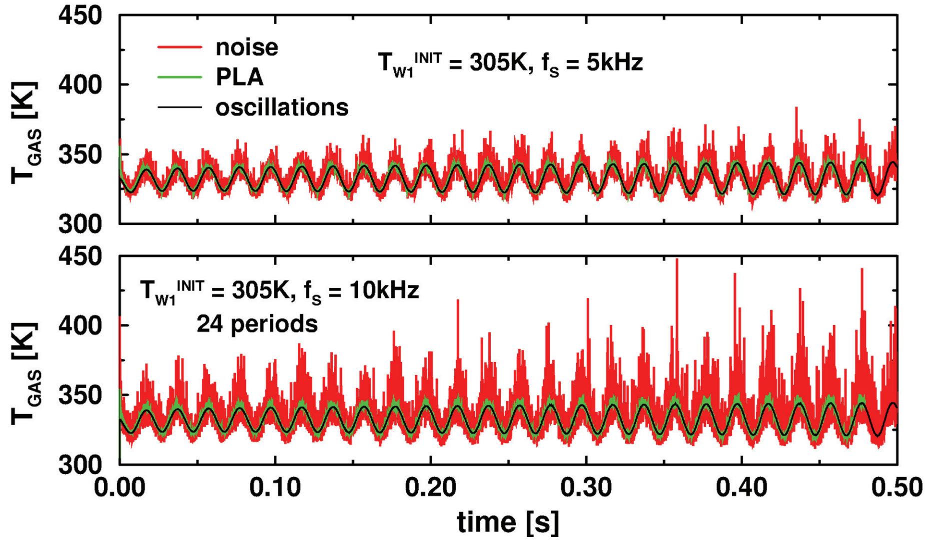

Figure 10-11: Case 1 and 3; noise reduction on the gas temperature calculations by phase locked averaging the noisy wall temperature

10.7 Calibration

Macor was selected for the material of the hemi-spherical heads because it is:

- a non-conductive material and therefore, not only the one dimensional assumption can be reassured for longer experimental times, but also the signal to noise ratio is improved;
- highly machinable and thus, finale small dimensions of the order of few tenths of mm on the heads designed are succeeded;
- not expensive;
- fully machined at VKI.

The need of measuring the thermal properties of the substrates of the gauges is of high importance. Assuming small temperature changes (less than *1K*) on the analytical approximation of the wall heat flux for a sphere in Eq. (37)), the wall heat flux is approximated to that on a flat surface. The general analytical wall heat flux solution for a flat plate in the Laplace domain (Eq. (7)) demonstrates that the wall heat flux strongly depends on the value of the thermal product of the substrate. Thus, for accurate heat flux calculations from the wall temperature signals the thermal product $(\rho ck)^{½}$ must be determined accurately.

For the specific case of the gas temperature calculations (Eq. (45)), only the wall heat fluxes ratio is necessary and not the absolute value of each one. The latter remark facilitates the thermal product calibration of the substrates of the two gauges: only a precise value of the thermal products ratio of the two substrates is essential for accurate gas temperature calculations.

The calibration procedure can be further facilitated, if both gauges are submitted under the same constant heat flux source. More specifically, a constant wall heat flux is also proportional to the gradient of temperature with respect to the square root of time (Eq. (9)). Measurements are therefore performed with both substrates at the same temperature, therefore exposed to the same wall heat flux. Applying (Eq. (9)) to the two substrates provides the ratio of both thermal products as a function of the two sensor temperature histories:

$$\frac{\sqrt{\rho c k_1}}{\sqrt{\rho c k_2}} = \frac{\left.\frac{\Delta T_W}{\sqrt{\Delta t}}\right|_2}{\left.\frac{\Delta T_W}{\sqrt{\Delta t}}\right|_1} = \frac{\left.\frac{\Delta T_W}{\sqrt{t-t_0}}\right|_2}{\left.\frac{\Delta T_W}{\sqrt{t-t_0}}\right|_1} \equiv \frac{slope_2}{slope_1} \quad . \tag{56}$$

The constant heat flux source used for the thermal products ratio calibration is a heated jet. The jet is a source of constant heat transfer coefficient rather than constant wall heat flux (paragraph 3.3.3). However, for short times (less than *0.05s*) the wall heat flux generated by the jet can be approximately considered as constant. In practice, the gauges are initially behind a shutter. Its opening in front of a hot air jet provides a step function in gas temperature on the two sensors.

The accurate determination of the time at which the sensors start to feel the flow, t_0, is of major importance. It is relatively easy to show that an error of *±5ms* in the determination of t_0 will be responsible for an error of *6%* on the ratio of the two thermal products. Thus, an iterative procedure that updates the t_0 till it converges is employed and showed graphically in Figure 10-12. First, an arbitrary choice of zero time is made (t_0 for the left top graph) and the gauge signal is reconstructed according to t_0 as a function of square root of time and is indicated with blue lines; the linear regressions (indicated with magenta lines) of the signal left and right to t_0 define a new time t_1. At the next iteration (right top graph), the linear regressions are performed around time t_1 and define t_2. The third and fourth iterations are shown at left and right bottom graphs respectively. Experience notifies that after three-four iterations, the value of t_0 is not far from that of the next iteration.

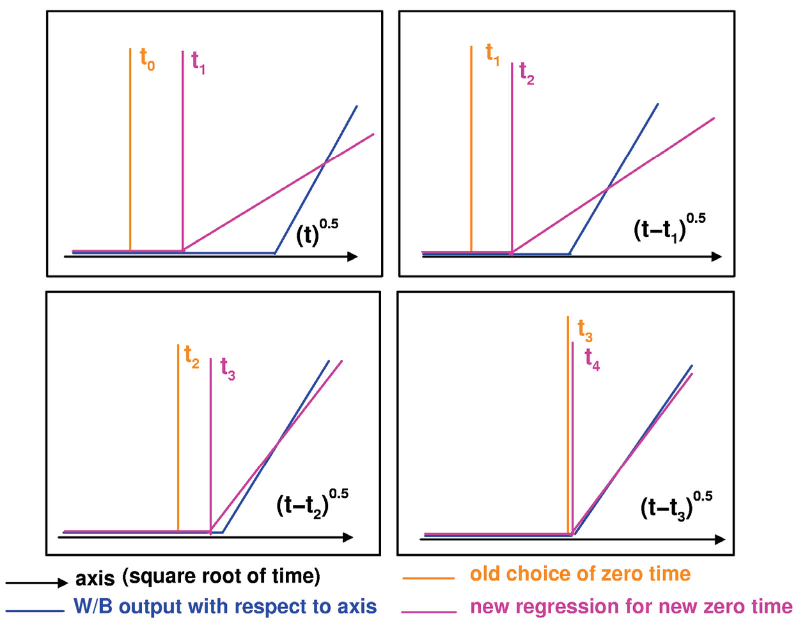

Figure 10-12: Graphical representation of the iterative procedure for the determination of the time t_0 when the sensors start to feel the flow

Typical signals from a calibration test are shown in Figure 10-13 as a function of time (top graph) and as a function of square root of time (bottom graph). The time t_0 is chosen slightly after the gauges start being heated by the jet and the beginning of the test (around t_0) seems to be highly perturbed, when the signals are plotted with square root of time. This perturbation mainly results from the fact that the generated wall heat flux is not a perfect step at t_0. This step is experimentally generated by the "fast" opening shutter (being initially closed between the nozzle exit and the gauges) that allows the heated jet to be applied on the gauges. However, the opening of the shutter is not instantaneous. Moreover, while the shutter is closed prior to the test, the flow is deflected and its establishment in the jet requires a minimum time.

The validity of Eq. (56) depends on the flat plate assumptions associated to Eq. (37)), i.e. low wall temperature variations (of the order of *1K*) or high relative values of the substrate radius of curvature. More specifically, in case of a sphere (*R=1.5mm*) made of Macor (*k=1.672W/(mK)*), the overestimation of the wall heat flux is around $1.1kW/m^2$ after *0.05s*. If the wall heat fluxes are calculated assuming the same thermal product for both gauges ($2073J/(m^2Ks^{0.5})$), this overestimation corresponds to a *7%* error of Eq. (56) (Figure 10-14).

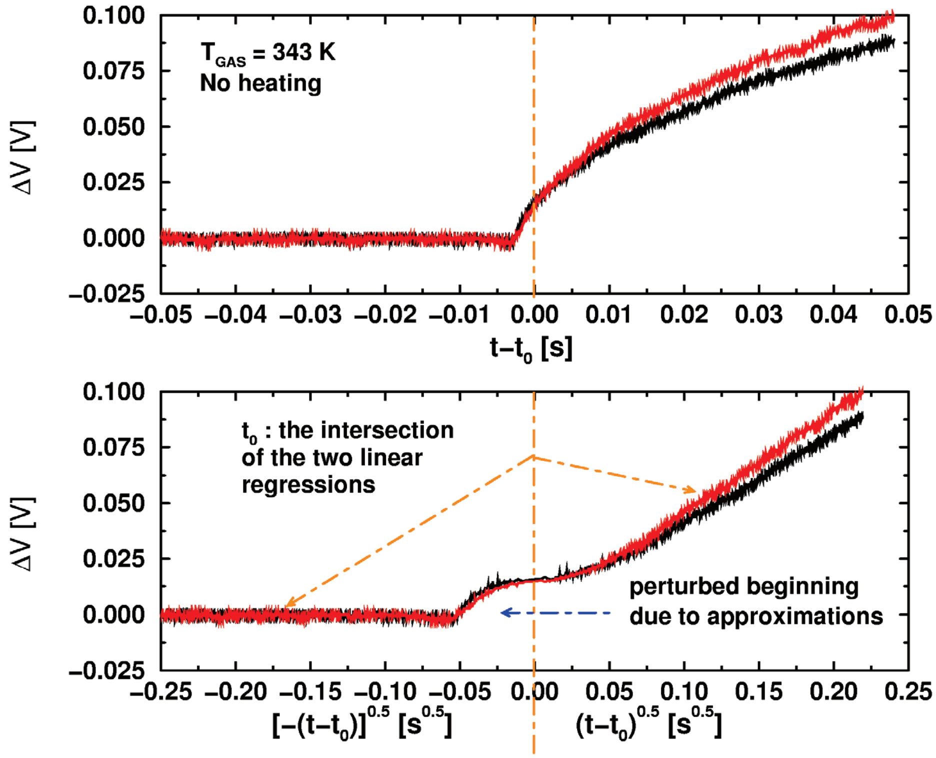

Figure 10-13: Signals from a calibration test

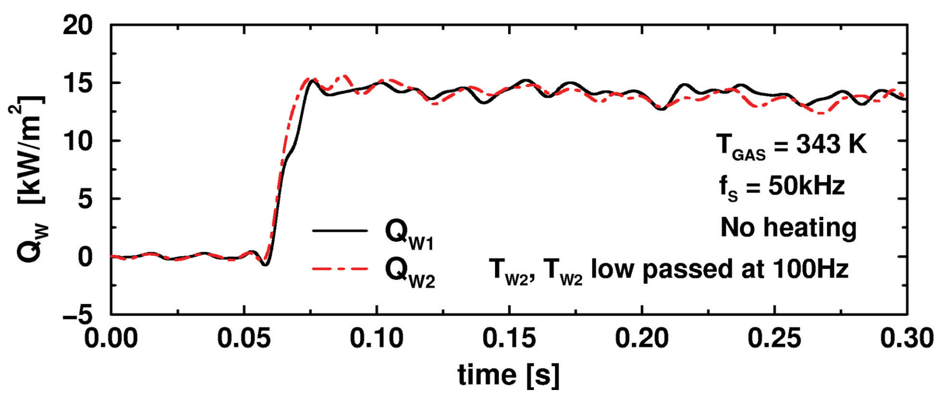

Figure 10-14: Wall heat fluxes from a calibration test

A second look on the wall heat fluxes of Figure 10-14 that are calculated through the numerical solution reveals that they are almost constant for a longer test time of *0.25s*. Thus, the second approximation that the hot jet generates constant wall heat fluxes, is not far from the reality.

A careful application of this technique allowed obtaining the value of the thermal product ratio of both substrates with an uncertainty less than *2%.* This uncertainty is principally due to the noise generated by the Wheatstone bridges, the determination of time t_0 and the quality of the applied heat flux step.

The calibration of the thermal products ratio of the two substrates is performed for both gauges under ambient initial wall temperatures. However, during a gas temperature measurement, a temperature difference is introduced by heating one of the two gauges. The influence of this temperature difference on the thermal products ratio can be considered negligible and it is further discussed in paragraph 15.1

10.8 References

Buttsworth D.R. & Jones T.V. (1998a): *A fast response total temperature probe for unsteady compressible flows.* ASME, J. of Engr. for Gas Turbines and Power, vol. 120, pp 694-702

Buttsworth D.R., Jones T.V., 1997, 'Radial conduction effects in transient heat transfer experiments', The aeronautical J., vol. May, pp 209-212

Buttsworth D.R., 1997, *'A finite difference routine for the solution of transient one dimensional heat conduction problems with curvature and thermal-dependent thermal properties'*, University of Oxford, OUEL Report number 2130/97

Denos R., 1996, *'Aerothermal investigation of the unsteady flow in the rotor of a transonic turbine stage'*, Ph.D. thesis, University of Poitiers, France

Iliopoulou V., Arts T., 2002, *'Applications of the heat flux thin film sensor in short duration flows'*, Proceedings of ESDA2002 ATF-040, Istanbul, Turkey

Kays W.M., Crawford M.E., 1980, 'Convective heat and mass transfer', McGraw-Hill, Inc, ISBN 0-07-033457-9, United States of America

Schultz D.L., Jones T.V., 1973, *'Heat transfer measurements in short duration hypersonic facilities'*, AGARDograph Report 165